Optimization of Multiphase Lattice Structures Subjected to Thermal and Mechanical Loads

Tong Wu
Ph.D. student
School of Mechanical Engr
Purdue University
West Lafayette, IN, USA
wu616@purdue.edu

Kai Liu
Ph.D. student
School of Mechanical Engr
Purdue University
West Lafayette, IN, USA
liu915@purdue.edu

Andres Tovar
Assistant Professor
Department of Mechanical Engineering
Indiana University-Purdue University Indianapolis
Indianapolis, IN, USA
tovara@iupui.edu

This work presents a design optimization approach to synthesize lightweight, multiphase lattice (porous) structures subjected to thermal and mechanical loads. A focus of this work is the design of plastic injection molds. The proposed approach seeks to minimize the injection mold mass while satisfying the targets of mechanical and thermal performance. The optimal tooling design is characterized by a quasi-periodic distribution of lattice unit-cells of variable relative density. The resulting complex design is suitable for fabrication using additive manufacturing technologies. The proposed structural optimization approach uses thermal and mechanical finite element analyses at two length scales: mesoscale and macroscale. At the mesoscale, lattice unit cells are analyzed in order to derive homogenized thermal and mechanical properties as a function of their relative density. At the mesoscale, the lattice unit cells are optimally distributed using these homogenized properties. The result is a multiphase cellular structure. The proposed structural optimization is a two-step approach. During the first step, the mass is minimized subject to constraints of mechanical compliance and thermal compliance. During the second step, lattice phases composed of cellular unit cells are optimally distributed subject to mechanical compliance, thermal compliance and non-convex functional constraints including maximum nodal temperature and displacement on the specific locations. The proposed design approach is demonstrated through 2D and 3D examples including the optimal design of an injection mold. The mold is fabricated using additive manufacturing. Examples show that a small reduction in mechanical and thermal performance allows for significant mass saving.

1 Introduction

Structure subjected to thermal and mechanical loads, such as injection molds, are required to maintain its mechanical stability (stiffness) during the injection molding cycle, withstanding pressure mechanical loads and thermal expansion, as well as transferring heat flux from the mold cavity to cooling channels filled with running coolant [1]. Unfortunately, traditional machining (subtractive) methods currently used in the fabrication of most injection tool limit the ability to fabricate such complex optimal designs. The rapid development of additive manufacturing (AM) technologies of metallic components offers the opportunity to create high performance injection tools at a reasonable cost [2–6]. A significant advantage of using AM to fabricate injection tooling is the ability to obtain lighter and more efficient molds and dies characterized by a complex internal structure. With the development of finite-element based structural optimization methods it is possible to improve the design of today's injection tool and create lightweight, innovative (complex) designs with higher thermomechanical performance.

Among currently available finite element-based design methods, topology optimization is recognized to provide innovative, high-performance layouts that are suitable to AM [7, 8]. Despite of their industrial relevance, mainstream topology optimization methods are restricted to provide a solid-void distribution of material without considering thermomechanical analysis. The objective of this work is to establish multiphase structural optimization approach of lattice injection tools suitable for AM. The use of optimized lattice cellular structures is an alternative to the traditional solid design that can be fabricated at a lower cost.

Integral to the proposed design process is the use of mul-

This is the author's manuscript of the article published in final edited form as:
Wu, T., Liu, K., & Tovar, A. (2017). Multiphase topology optimization of lattice injection molds. Computers & Structures, 192, 71–82.
https://doi.org/10.1016/j.compstruc.2017.07.007

tiscale thermomechanical analysis along with asymptotic homogenization methods for mechanical and thermal properties. With respect to thermomechanical analysis, mechanical topology optimization with the consideration of thermal expansion has been used in the micro-electro-mechanical-systems (MEMS) [7]. Thermal expansion has been also considered in the topology optimization of electronic packages to minimize the harmful stress between the different layers caused by the different thermal expansion coefficients of layered materials [9]. Topology optimization with reference to heat conduction has been employed to minimize the temperature gradient magnitude distribution (heat dissipation) for thermal components including heat sinks for multichip modules [10] and thermal-fluid electronic microchannels [11]. Studies that consider coupled heat conduction and linear elasticity in the topology optimization have been recently proposed [12]; however, the studies are limited to 2D solid-void structures.

With respect to multiscale topology optimization, asymptotic homogenization methods have been used to derive macroscale mechanical properties of components composed of cellular or composite 3D meso-structures [13]. Multiscale topology optimization methods have been traditionally addressed by addressing the optimal topology of the structure and the optimal design of the cellular material. This strategy has been successfully applied to 3D structural problems. Despite of its potential, this approach has two main drawbacks. First, it requires the execution of several problems in parallel for each iteration, which makes it computationally expensive, especially for 3D designs, and parallel computing may be required. Second, this approach does not necessarily converge to a manufacturable, connected microstructural design and time-consuming post-processing may be needed. An alternative multiscale topology optimization approach, namely multiphase topology optimization, consists on interpolating homogenized material properties of a multiple priori-defined cellular unit cells [14, 15]. The shape of the materials is regular and controlled by a few of geometric parameters that define a potentially large range porosity. The material interpolation is modified to guide a macroscale structure consisting of only the discrete set of a priori set of given unit cells. Under 2D plane stress assumption, this approach has been useful to generate quasi-periodic cellular structures suitable for additive manufacturing. Multiscale topology optimization used to derive macroscale thermal properties of components is not commonly found in literature.

In this paper, a multiphase thermomechanical approach is proposed in 3D topology optimization. Asymptotic homogenization methods are implemented for isotropic thermal conductivity and orthotropic linear elasticity. The results are demonstrated with the topology optimization of lattice structures with minimum mass under elastic mechanical and thermal constraints.

2 Overview of the proposed structural optimization approach

The proposed optimization approach involves structures in two length-scales: mesoscale and macroscale. In the mesoscale, lattice unit cells are analyzed in order to homogenize their thermomechanical properties. As a result, homogenized elastic and thermal coefficients are expressed as functions of the volume fraction of the lattice unit cell. In the macroscale, the structural optimization problem is solved and the lattice unit cells are optimally distributed. The macroscale contains injection tool's boundary conditions including the external mechanical loads as well as the heat sources and sinks in the form of a mold cavity and cooling channels. The macroscale design problem addressed in this work is to find the optimal distribution of given number of lattice phases within the component so its mass is minimized while satisfying stiffness and heat conduction constraints of the overall component and the specific regions.

The macroscale problem is solved in two steps: First, a relaxed convex problem is addressed so that the mass is minimized subject to constraints on mechanical compliance and a thermal compliance [16]. Second, based on the conceptual design from the first step, the algorithm finds the optimal distribution of a discrete number of lattice unit cells (phases) so that the maximum displacement and temperature are minimized in specific locations of the injection tool. The optimization approach is summarized in Fig. 1.

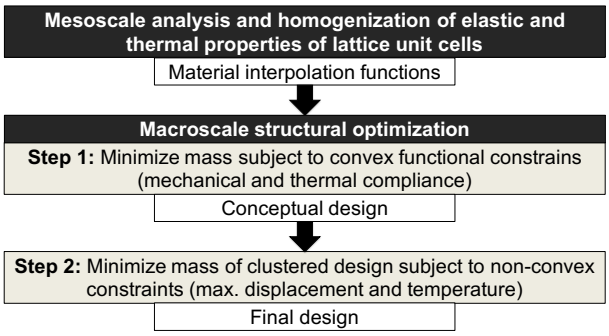

Fig. 1. Flowchart of proposed design approach.

3 Mesoscale analysis and homogenization of elastic and thermal properties of lattice unit cells

This section summarizes the numerical approaches used to derive the homogenized elasticity tensor $\mathbf{D}_c^H$ and the homogenized thermal conductivity tensor $\boldsymbol{\kappa}_c^H$ of an a-priori defined lattice unit cell. The theory summarized in this section follows the principles of asymptotic homogenization [17–19].

3.1 Asymptotic homogenization of the elastic properties

Let a macroscale design domain Ω to be comprised of n_c unit cells, where $c = 1, \ldots, n_c$. Each unit cell is further

discretized into n_e finite elements as illustrated in Fig. 2.

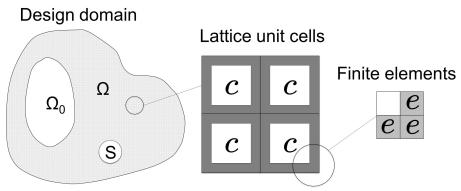

Fig. 2. Hierarchical organization of the design domain.

According to the homogenization theory for media with a periodic structure, the homogenized elasticity tensor $\mathbf{D}_c^H$ of a discretized periodic unit cell is given by

$$\mathbf{D}_c^H = \frac{1}{|V_c|}\sum_{e=1}^{n_e}\int_{V_e}[\mathbf{I}-\mathbf{B}_e\boldsymbol{\chi}_e]^\intercal\mathbf{D}_e[\mathbf{I}-\mathbf{B}_e\boldsymbol{\chi}_e]\mathrm{d}V_e, \quad (1)$$

where n_e are the number of finite elements of the discretized unit cell, $|V_c|$ is the unit cell volume, $\mathbf{I}$ is the identity matrix, V_e is the volume of the finite element e, $\mathbf{B}_e$ is the element strain-displacement matrix, $\mathbf{D}_e$ is the element elasticity tensor, and $\boldsymbol{\chi}_e$ is the matrix containing the element displacement vectors $\boldsymbol{\chi}_e^{ij}$ resulting from globally enforcing the unit test strains $\boldsymbol{\varepsilon}^{ij}$ (Fig. 3). For a 3D solid finite element, this is

$$\boldsymbol{\chi}_e = [\boldsymbol{\chi}_e^{11},\boldsymbol{\chi}_e^{22},\boldsymbol{\chi}_e^{33},\boldsymbol{\chi}_e^{12},\boldsymbol{\chi}_e^{23},\boldsymbol{\chi}_e^{13}], \quad (2)$$

where $\boldsymbol{\chi}_e^{ij}$ are vectors of size 24×1. The element displacement vectors $\boldsymbol{\chi}_e^{ij}$ are obtained from the global displacement vector of the unit cell $\boldsymbol{\chi}_c^{ij}$, which is the solution of the equilibrium equation

$$\left[\sum_{e=1}^{n_e}\int_{V_e}\mathbf{B}_e^\intercal\mathbf{D}_e\mathbf{B}_e\mathrm{d}V_e\right]\boldsymbol{\chi}_c^{ij} = \sum_{e=1}^{n_e}\int_{V_e}\mathbf{B}_e^\intercal\mathbf{D}_e\boldsymbol{\varepsilon}^{ij}\mathrm{d}V_e. \quad (3)$$

The first term in the left hand side of Eq. (3) is the stiffness matrix of the unit cell and the right hand side is the nodal force vector of the unit cell.

It is convenient to define the element nodal displacement matrix $\boldsymbol{\chi}_e^0$ within a solid isotropic cell. This isotropic nodal displacement matrix is the solution of the equilibrium equation

$$\mathbf{B}_e\boldsymbol{\chi}_e^0 = \mathbf{I}. \quad (4)$$

Since $\mathbf{I} = [\boldsymbol{\varepsilon}^{11},\boldsymbol{\varepsilon}^{22},\boldsymbol{\varepsilon}^{33},\boldsymbol{\varepsilon}^{12},\boldsymbol{\varepsilon}^{23},\boldsymbol{\varepsilon}^{13}]$, then Eq. (4) can be written as

$$\left[\int_{V_e}\mathbf{B}_e^\intercal\mathbf{D}_e\mathbf{B}_e\mathrm{d}V_e\right]\boldsymbol{\chi}_e^{0(ij)} = \int_{V_e}\mathbf{B}_e^\intercal\mathbf{D}_e\boldsymbol{\varepsilon}^{ij}\mathrm{d}V_e. \quad (5)$$

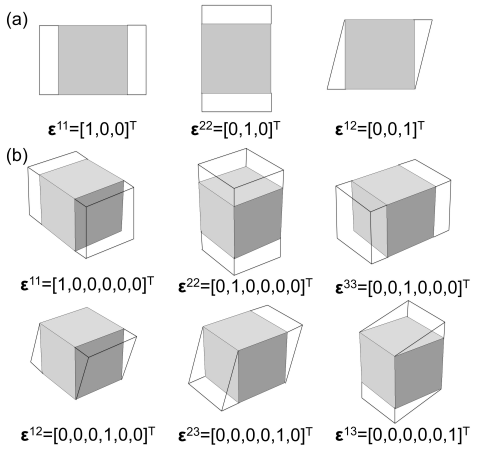

Fig. 3. The chosen unit strain tests imposed on (a) 2D representative unit cells and (b) 3D representative unit cells.

Therefore, each component of the homogenized elasticity tensor $\mathbf{D}_c^H$ can be expressed as

$$D_{c,ijkl}^H = \frac{1}{|V|}\sum_{e=1}^{n_e}\int_{V_e}[\boldsymbol{\chi}_e^{0(ij)}-\boldsymbol{\chi}_e^{ij}]^\intercal\mathbf{k}_e[\boldsymbol{\chi}_e^{0(kl)}-\boldsymbol{\chi}_e^{kl}]\mathrm{d}V_e, \quad (6)$$

where $\mathbf{k}_e$ is the stiffness matrix for an element. The homogenized elasticity tensor is obtained based on periodic boundary conditions. For a 3D unit cell, this tensor is a symmetric matrix of the form

$$\mathbf{D}_c^H = \begin{bmatrix} D_{c,1111}^H & D_{c,1122}^H & D_{c,1133}^H & D_{c,1112}^H & D_{c,1123}^H & D_{c,1113}^H \\ D_{c,2211}^H & D_{c,2222}^H & D_{c,2233}^H & D_{c,2212}^H & D_{c,2223}^H & D_{c,2213}^H \\ D_{c,3311}^H & D_{c,3322}^H & D_{c,3333}^H & D_{c,3312}^H & D_{c,3323}^H & D_{c,3313}^H \\ D_{c,1211}^H & D_{c,1222}^H & D_{c,1233}^H & D_{c,1212}^H & D_{c,1223}^H & D_{c,1213}^H \\ D_{c,2311}^H & D_{c,2322}^H & D_{c,2333}^H & D_{c,2312}^H & D_{c,2323}^H & D_{c,2313}^H \\ D_{c,1311}^H & D_{c,1322}^H & D_{c,1333}^H & D_{c,1312}^H & D_{c,1323}^H & D_{c,1313}^H \end{bmatrix}. \quad (7)$$

Each coefficient $D_{c,ijkl}^H$ can be expressed as a function of the density of the unit cell as explained later in this paper.

3.2 Asymptotic homogenization of the thermal conductivity

Following the homogenization theory for thermal conductivity [19], the homogenized thermal conductivity tensor $\boldsymbol{\kappa}_c^H$ of a discretized periodic unit cell is given by

$$\boldsymbol{\kappa}_c^H = \frac{1}{|V_c|}\sum_{e=1}^{n_e}\int_{V_e}[\mathbf{I}-\mathbf{B}_e^t\mathbf{T}_e]^\intercal\boldsymbol{\kappa}_e[\mathbf{I}-\mathbf{B}_e^t\mathbf{T}_e]\mathrm{d}V_e, \quad (8)$$

where n_e are the number of finite elements of the discretized unit cell, $|V_c|$ is the unit cell volume, $\mathbf{I}$ is the identity matrix, V_e is the volume of the finite element, $\mathbf{B}_e^t$ is the element "strain" (temperature gradient)-temperature matrix, $\boldsymbol{\kappa}_e$ is the element thermal conductivity tensor, and $\mathbf{T}_e$ is the matrix containing the element nodal temperature vectors $\mathbf{T}_e^{ij}$ re-

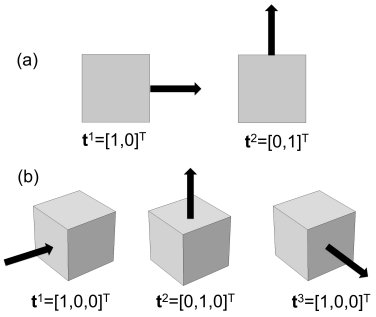

Fig. 4. Unit temperature gradients imposed on (a) 2D representative unit cells and (b) 3D representative unit cells.

sulting from globally enforcing the unit test temperature gradients $\mathbf{t}^i$ (Fig. 4). For a 3D solid finite element, this is

$$\mathbf{T}_e = [\mathbf{T}_e^1, \mathbf{T}_e^2, \mathbf{T}_e^3], \tag{9}$$

where the size of the vectors $\mathbf{T}_e^i$ is 8×1. As before, the element temperature vectors $\mathbf{T}_e^i$ are obtained from the global temperature vector of the unit cell $\mathbf{T}_c^i$, which is the solution of the equilibrium equation

$$\left[\sum_{e=1}^{n_e} \int_{V_e} \mathbf{B}_e^{t\,\intercal} \boldsymbol{\kappa}_e \mathbf{B}_e^t \mathrm{d}V_e\right] \mathbf{T}_c^i = \sum_{e=1}^{n_e} \int_{V_e} \mathbf{B}_e^{t\,\intercal} \boldsymbol{\kappa}_e \mathbf{t}^i \mathrm{d}V_e. \tag{10}$$

The first term in the left hand side of Eq. (10) is the "stiffness" thermal matrix of the unit cell and the right hand side is the nodal heat flux vector of the unit cell.

The element nodal temperature matrix $\mathbf{T}_e^0$ within a solid isotropic (solid) cell is the solution of the equilibrium equation

$$\mathbf{B}_e^t \mathbf{T}_e^0 = \mathbf{I}. \tag{11}$$

Since $\mathbf{I} = [\mathbf{t}^1, \mathbf{t}^2, \mathbf{t}^3]$, then Eq. (11) can be written as

$$\left[\int_{V_e} \mathbf{B}_e^{t\,\intercal} \boldsymbol{\kappa}_e \mathbf{B}_e^t \mathrm{d}V_e\right] \mathbf{T}_e^{0(i)} = \int_{V_e} \mathbf{B}_e^{t\,\intercal} \boldsymbol{\kappa}_e \mathbf{t}^i \mathrm{d}V_e. \tag{12}$$

Therefore, each component of the homogenized stiffness thermal tensor $\boldsymbol{\kappa}_c^H$ can be expressed as

$$\kappa_{c,ij}^H = \frac{1}{|V_c|} \sum_{e=1}^{n_e} \int_{V_e} [\mathbf{T}_e^{0(i)} - \mathbf{T}_e^i]^\intercal \mathbf{k}_e^t [\mathbf{T}_e^{0(j)} - \mathbf{T}_e^j] \mathrm{d}V_e, \tag{13}$$

where $\mathbf{k}_e$ is the stiffness thermal matrix for an element. For a 3D unit cell, this tensor is a symmetric matrix of the form

$$\boldsymbol{\kappa}_c^H = \begin{bmatrix} \kappa_{c,11}^H & \kappa_{c,12}^H & \kappa_{c,13}^H \\ \kappa_{c,21}^H & \kappa_{c,22}^H & \kappa_{c,23}^H \\ \kappa_{c,31}^H & \kappa_{c,32}^H & \kappa_{c,33}^H \end{bmatrix}. \tag{14}$$

Here as well, each coefficient $\kappa_{c,ij}^H$ can be expressed as a function of the relative density of the unit cell as explained in the following section.

3.3 Interpolation of homogenized thermomechanical properties

For a given set of lattice unit cells with known relative density values θ_c', the homogenized elasticity tensors $\mathbf{D}_c^H$ and the homogenized thermal conductivity tensors $\boldsymbol{\kappa}_c^H$ are obtained. Then, an interpolation function is derived to correlate the relative density θ_c of the unit cell with its corresponding homogenized tensor coefficients. Using a polynomial approximation, the elasticity tensor coefficients are expressed as follows:

$$D_{c,ijkl}^H(\theta) = a_0 + \sum_{q=1}^{n_q} a_q \theta^q + \mathscr{O}(\theta^{n_q+1}), \tag{15}$$

where the coefficients a_q, for $q = 0, \ldots, n_q$, are determined by polynomial regression. Similarly, for the components of the homogenized thermal conductivity tensor, one obtains that

$$\kappa_{c,ij}^H(\theta) = b_0 + \sum_{q=1}^{n_q} b_q \theta^q + \mathscr{O}(\theta^{n_q+1}). \tag{16}$$

Polynomials of order one (linear interpolations) can also be obtained with $a_0 = 0$ and $a_1 = D_{c,ijkl}^H(\theta_c' = 1)$ for the elasticity tensor, and $b_0 = 0$ and $b_1 = \kappa_{c,ij}^H(\theta_c' = 1)$ for the thermal conductivity tensor. These interpolations are inaccurate but make the optimization problem convex; hence, they are utilized to generate the conceptual design (Step 1) (Sec. 4.1). Polynomials of order three are shown to provide sufficient accuracy and are used in the final stage of the optimization process (Step 2) (Sec. 4.2).

4 Macroscale structural optimization

The proposed multiphase structural optimization approach consists of two steps. During the first step, an initial (conceptual) optimal distribution of unit cell relative densities θ_{1c}^*, $c = 1, \ldots, n_c$ is obtained. The conceptual design minimizes the mass of the structure subject to two functional constraints: mechanical compliance and thermal compliance. A linear interpolation of the elastic coefficients and thermal conductivity is used to make the problem convex. During the second step, the relative density values are optimally clustered using a set of predefined values θ_p', $p = 1, \ldots, n_p$. The clustering process results in a design that can be easily fabricated using AM techniques. The final optimal design θ_{2c}^* minimizes the mass of the structure subject to constraints of the maximum displacement and temperature in specific regions of the design domain. The design domain Ω contains the cavities Ω_0 and heat sinks S of the injection tool to be optimized as well as the mechanical loads $\mathbf{f}$, supports, heat flux $\mathbf{q}$, and insulated boundaries. Also, let's define the

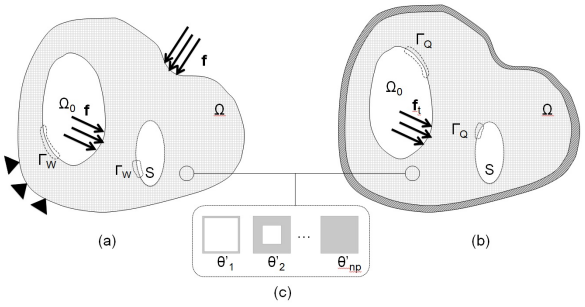

Fig. 5. The macroscale design domain: (a) mechanical boundary conditions, (b) thermal boundary conditions, and (c) finite number of lattice unit cells to be optimally distributed.

boundaries Γ_W with target of the maximum displacement, and boundaries Γ_Q with target of the maximum temperature (Fig. 5).

In each step, the optimization is performed using the Globally Convergence Method of Moving Asymptotes (GCMMA) algorithm implemented in the FEA software COMSOL Multiphysics (COMSOL, Stockholm, Sweden). The convergence ε in the GCMMA algorithm is given by the following condition:

$$\varepsilon = \left| \frac{\partial \psi(\boldsymbol{\lambda})}{\partial \lambda_i} \right| \leq \varepsilon_g, \tag{17}$$

where $\psi(\boldsymbol{\lambda})$ is the dual objective function, $\boldsymbol{\lambda}$ is the vector of Lagrange multipliers, and ε_g is a small positive number [20]. By default, $\varepsilon_g = 10^{-6}$ for the following 2D examples and $\varepsilon_g = 10^{-3}$ for the following 3D examples. Another convergence criterion is the number of maximum objective function evaluations N. By default, $N = 500$ for the following 2D examples and $N = 150$ for the following 3D examples.

4.1 Step 1: Minimize mass subject to convex functional constrains

The first step aims to find the relative densities $\boldsymbol{\theta} \in \mathbb{R}^{n_c}$ that minimizes the structure's mass $m(\boldsymbol{\theta})$, subject to mechanical compliance and thermal compliance constraints of the design domain. The mass of the structure is defined by

$$m(\boldsymbol{\theta}) = \gamma_0 \sum_{c=1}^{n_c} v_c \theta_c, \tag{18}$$

where v_c is the element (unit cell) volume and γ_0 is the base material density. Mechanical compliance reflects the average displacement of the structure. In matrix notation, the mechanical compliance is defined as

$$W = \int_\Omega \boldsymbol{\varepsilon}^\intercal \mathbf{D}^H \boldsymbol{\varepsilon} \mathrm{d}\Omega, \tag{19}$$

where $\mathbf{D}^H$ is the homogenized elasticity tensor and $\boldsymbol{\varepsilon}$ is the strain tensor. An appropriate mechanical compliance constraint ensures the structure deformation is small and the linear FEA is feasible. Similarly, the thermal compliance reflects the average temperature of the whole structure. It is defined as

$$Q = \int_\Omega \mathbf{t}^\intercal \boldsymbol{\kappa}^H \mathbf{t} \mathrm{d}\Omega, \tag{20}$$

where $\boldsymbol{\kappa}^H$ is the homogenized thermal conductivity tensor and $\mathbf{t}$ indicates temperature gradients. This constraint determines the compromise of heat conduction performance of the whole structure. With the discretization of the macroscale domain and the application of finite element analysis (FEA), the equation (19) yields the quadratic form

$$W(\boldsymbol{\theta}) = \mathbf{f}^\intercal \mathbf{u}(\boldsymbol{\theta}), \tag{21}$$

where $\mathbf{f}$ is the vector of external loads and $\mathbf{u}(\boldsymbol{\theta})$ is the vector of nodal displacements in the macroscale domain. The vector of nodal displacements satisfies the Hooke's law equilibrium equation:

$$\mathbf{K}(\boldsymbol{\theta})\mathbf{u}(\boldsymbol{\theta}) = \mathbf{f}, \tag{22}$$

where

$$\mathbf{K}(\boldsymbol{\theta}) = \sum_{c=1}^{n_c} \int_{V_c} \mathbf{B}_c^\intercal \mathbf{D}_c^H(\theta_c) \mathbf{B}_c \mathrm{d}V_c. \tag{23}$$

In Eq. (23), $\mathbf{K}(\boldsymbol{\theta})$ is the stiffness matrix of the macroscale domain, $\mathbf{B}_c$ represents the strain-displacement relations of a unit cell, and $\mathbf{D}_c^H(\theta_c)$ is the homogenized elasticity tensor of a unit cell. In the same way, the thermal compliance (20) yields the quadratic form

$$Q(\boldsymbol{\theta}) = \mathbf{q}^\intercal \mathbf{T}(\boldsymbol{\theta}), \tag{24}$$

where $\mathbf{q}$ is the boundary heat flux and $\mathbf{T}(\boldsymbol{\theta})$ is the vector of nodal temperatures in the macroscale design domain. The vector of nodal temperatures satisfies the Fourier's law equilibrium equation:

$$\mathbf{K}_t(\boldsymbol{\theta})\mathbf{T}(\boldsymbol{\theta}) = \mathbf{q}, \tag{25}$$

where

$$\mathbf{K}_t(\boldsymbol{\theta}) = \sum_{c=1}^{n_c} \int_{V_c} \mathbf{B}_c^{t\,\intercal} \boldsymbol{\kappa}_c^H(\theta_c) \mathbf{B}_c^t \mathrm{d}V_c. \tag{26}$$

In Eq. (26), $\mathbf{K}_t(\boldsymbol{\theta})$ is the thermal stiffness matrix of macroscale domain, $\mathbf{B}_c^t$ is the temperature and temperature gradient

relations of a unit cell, and $\boldsymbol{\kappa}_c^H(\theta_c)$ is the homogenized thermal conductivity tensor of a unit cell.

Finally, the first optimization problem is stated as follows:

$$\begin{aligned}
\text{find} \quad & \boldsymbol{\theta}_1^* \in \mathbb{R}^{n_c} \\
\text{minimize} \quad & J_1(\boldsymbol{\theta}_1) = m(\boldsymbol{\theta}_1)/m(\boldsymbol{\theta}_0) \\
\text{subject to} \quad & W(\boldsymbol{\theta}_1) = \mathbf{f}^\intercal \mathbf{u}(\boldsymbol{\theta}_1) \leq C_W W(\boldsymbol{\theta}_0) \\
& Q(\boldsymbol{\theta}_1) = \mathbf{q}^\intercal \mathbf{T}(\boldsymbol{\theta}_1) \leq C_Q Q(\boldsymbol{\theta}_0) \\
& \boldsymbol{\theta}^{\min} \leq \boldsymbol{\theta}_1 \leq \mathbf{1} \\
\text{satisfying} \quad & \mathbf{u}(\boldsymbol{\theta}_1) = \mathbf{K}(\boldsymbol{\theta}_1)^{-1}\mathbf{f} \\
& \mathbf{T}(\boldsymbol{\theta}_1) = \mathbf{K}_t(\boldsymbol{\theta}_1)^{-1}\mathbf{q}
\end{aligned} \tag{27}$$

where $\boldsymbol{\theta}_0$ represents the initial solid structure, $\theta_{0c} = 1$ for $c = 1, \ldots, n_c$, $m(\boldsymbol{\theta}_0)$ is the initial mass, and $C_W \geq 1$ and $C_Q \geq 1$ are coefficients that degrade the mechanical compliance and thermal compliance of the initial design—by increasing these coefficients, the mass of the structure decreases and the performance of structure is sacrificed. The lower bound $\boldsymbol{\theta}^{\min}$ prevents the singularity of $\mathbf{K}(\boldsymbol{\theta}_1)$ and $\mathbf{K}_t(\boldsymbol{\theta}_1)$ and also prevents voids within the cellular structure. The value of the lower bound is also determined by the resolution of the AM system (3D printer). In this work, $\theta_c^{\min} = 0.259$ for 3D and $\theta_c^{\min} = 0.190$ for 2D, for $c = 1, \ldots, n_c$. Linear material interpolation functions connecting the homogenized properties of $\theta_c^{\min}$ and the solid material properties are used, in order to interpolate $\mathbf{D}_c^H(\theta_c)$ in $\mathbf{K}(\boldsymbol{\theta}_1)$ and $\boldsymbol{\kappa}_c^H(\theta_c)$ in $\mathbf{K}_t(\boldsymbol{\theta}_1)$. In this way, the material properties deviate the real values, but it ensures the problem is convex and the mass is the global minimum. The results of this design step can be used as the initial design and the baselines of the second design step.

4.2 Step 2: Minimize mass of a clustered design subject to non-convex functional constraints

The objective of the second step is to minimize the structure's mass $m(\boldsymbol{\theta})$ subject to five constraints. The three constraints used in the last step are also needed to be satisfied. Besides, two additional non-convex functional constraints are required, which are maximum displacement $U(\boldsymbol{\theta}_2)$ and temperature $T(\boldsymbol{\theta}_2)$ in specific locations of the design domain (Γ_W and Γ_Q):

$$\begin{aligned}
U(\boldsymbol{\theta}_2) &= \max_{u_j \in \Gamma_W} \{u_j(\boldsymbol{\theta}_2)\} \leq C_U U^{\max}(\boldsymbol{\theta}_0) \\
T(\boldsymbol{\theta}_2) &= \max_{T_j \in \Gamma_Q} \{T_j(\boldsymbol{\theta}_2)\} \leq C_T T^{\max}(\boldsymbol{\theta}_0).
\end{aligned} \tag{28}$$

These locations can be the surface of heat source or cooling pipe of a mold, where the displacement and temperature needed to be controlled within a strict threshold, in order to guarantee the performance of the mold. The upper bounds of $U(\boldsymbol{\theta}_2)$ and $T(\boldsymbol{\theta}_2)$ are the values corresponding of a solid structure times coefficient C_U and C_T, respectively, where $C_U, C_T \geq 1$. Since these two constraints are satisfied in a solid design, they will not be violated.

The objective function is also modified to avoid mesh dependency and highly varied densities, in order to create a multiphase material distribution that can be efficiently mapped to a manufacturable lattice strucuture. A gradient control regularization function $R(\boldsymbol{\theta})$ is added to the objective to provide mesh-independent a result and improve the manufacturability [21]. This function is defined as follows:

$$R(\boldsymbol{\theta}) = \sum_{c=1}^{n_c} \nabla\theta_c{}^\intercal \nabla\theta_c, \tag{29}$$

where $\nabla\theta_c$ is the spatial gradient of the design variable field evaluated at the discrete location c. The intermediate densities caused by the addition of this regularization function are clustered using the following penalization function:

$$\begin{aligned}
P(\boldsymbol{\theta}, \boldsymbol{\theta}') &= \sum_{c=1}^{n_c} |\theta_c - \theta_1'| \cdot |\theta_c - \theta_2'| \cdots |\theta_c - \theta_{n_p}'| \\
&= \sum_{c=1}^{n_c} \prod_{p=1}^{n_p} |\theta_c - \theta_p'|,
\end{aligned} \tag{30}$$

where θ_p' are predefined relative density values. A small value $P(\boldsymbol{\theta}, \boldsymbol{\theta}')$ ensures the design can be represented by a discrete number n_p of unit cells phases [21]. The penalization function in Eq. (30) is also added to the objective function.

Finally, the optimization problem is defined as follows:

$$\begin{aligned}
\text{find} \quad & \boldsymbol{\theta}_2^* \in \mathbb{R}^{n_c} \\
\text{minimize} \quad & J(\boldsymbol{\theta}_2) = \frac{m(\boldsymbol{\theta}_2)}{m(\boldsymbol{\theta}_1^*)} + C_R R(\boldsymbol{\theta}_2) + C_P \frac{P(\boldsymbol{\theta}_2, \boldsymbol{\theta}')}{P(\boldsymbol{\theta}_1^*, \boldsymbol{\theta}')} \\
\text{subject to} \quad & W(\boldsymbol{\theta}_2) = \mathbf{f}^\intercal \mathbf{u}(\boldsymbol{\theta}_2) \leq C_W W(\boldsymbol{\theta}_0) \\
& Q(\boldsymbol{\theta}_2) = \mathbf{q}^\intercal \mathbf{T}(\boldsymbol{\theta}_2) \leq C_Q Q(\boldsymbol{\theta}_0) \\
& U(\boldsymbol{\theta}_2) = \max_{u_j \in \Gamma_W} \{u_j(\boldsymbol{\theta}_2)\} \leq C_U U^{\max}(\boldsymbol{\theta}_0) \\
& T(\boldsymbol{\theta}_2) = \max_{T_j \in \Gamma_Q} \{T_j(\boldsymbol{\theta}_2)\} \leq C_T T^{\max}(\boldsymbol{\theta}_0) \\
& \boldsymbol{\theta}^{\min} \leq \boldsymbol{\theta}_2 \leq \mathbf{1} \\
\text{satisfying} \quad & \mathbf{u}(\boldsymbol{\theta}_2) = \mathbf{K}(\boldsymbol{\theta}_2)^{-1}\mathbf{f} \\
& \mathbf{T}(\boldsymbol{\theta}_2) = \mathbf{K}_t(\boldsymbol{\theta}_2)^{-1}\mathbf{q}
\end{aligned} \tag{31}$$

where the coefficients C_R and C_P are small positive numbers, $C_R < 1$ and $C_P < 1$. The upper bound of $U(\boldsymbol{\theta})$ is the maximum displacement $U^{\max}$ in Γ_W of a solid structure times a coefficient C_U, and the upper bound of $T(\boldsymbol{\theta})$ is the maximum temperature $T^{\max}$ in Γ_Q of a solid structure times a coefficient C_T, where $C_U, C_T \geq 1$. Since these two constraints are satisfied in a solid design, they will not be violated.

Polynomials material interpolation function of order three (Sec. 3.3) are used to interpolate $\mathbf{D}_c^H(\theta_c)$ in $\mathbf{K}(\boldsymbol{\theta}_2)$ and $\boldsymbol{\kappa}_c^H(\theta_c)$ in $\mathbf{K}_t(\boldsymbol{\theta}_2)$. The next section shows numerical examples of the proposed design approach.

5 Numerical examples

Two examples are presented to illustrate the design approach. The first example consists of the design of a multiphase 2D plate in cantilever thermo-mechanically loaded. The second example is the design of the cavity and core plates of a multiphase 3D plastic injection mold. In both examples, the properties of the base material are: density $\gamma_0 = 7850$ kg/m^3, Young's modulus $E_0 = 200$ GPa, Poisson's ratio $\nu_0 = 0.3$. In the first example, thermal conductivity $\kappa_0 = 44.5$ W/(m·K) is taken, but in the second example, $\kappa_0 = 17.8$ W/(m·K) is taken, which is the thermal conductivity of A286 stainless steel alloy at $573.15K$.

5.1 Design of a multiphase thermomechanically-loaded 2D plate

Let us consider a square plate of dimensions 1 m $\times$ 1 m and thickness 1 cm. The plate is rigidly fixed along its left lateral side as shown in Fig. 6(a). A downward force $F = 1$ kN is applied at the lower right corner. A heat sink with constant temperature 0°C (273.15 K) is located at the center of the left lateral side as shown in Fig. 6(b). All other sides of the plate are insulated. A heat flux $q = 10$ W is uniformly distributed on the plate's body. The plate is discretized into 2453 quadrilateral elements. The nodal displacement distributions under plane stress analysis and the nodal temperature distributions from FEA are shown in Figs. 6(c) and (d), respectively. In this example, the mechanical compliance $W(\boldsymbol{\theta})$, the thermal compliance $Q(\boldsymbol{\theta})$, the maximum displacement $U(\boldsymbol{\theta})$ on the surface Γ_W, and the maximum temperature $T(\boldsymbol{\theta})$ on the surface Γ_Q are listed in Tab. 1 (a). Γ_W corresponds to the heat sink surface, and Γ_Q corresponds to the right free end of the plate.

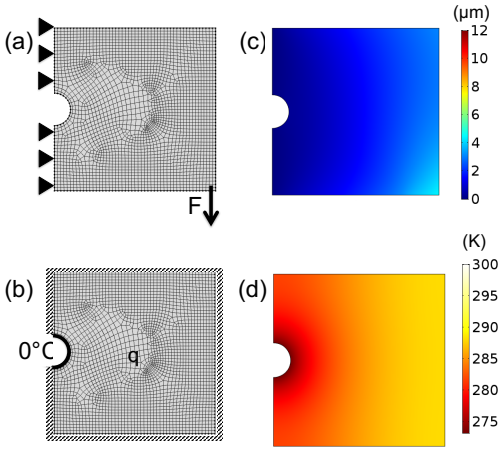

Fig. 6. Boundary conditions and results of the FEA for a plate: (a) mechanical load and supports; (b) thermal heat flux, sink, and insulation; (c) nodal displacement; and (d) nodal temperature distribution.

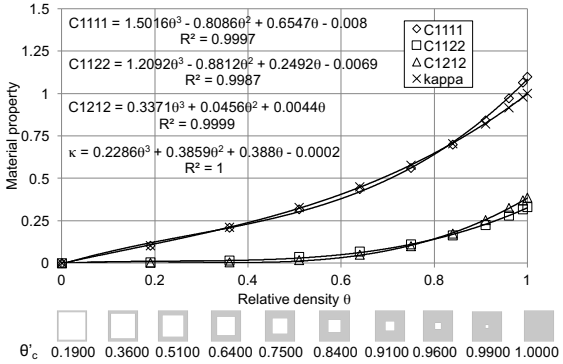

Fig. 7. Interpolation of elasticity coefficients and thermal conductivity for 2D unit cells.

5.1.1 Mesoscale analysis and homogenization

For the interpolation of the elastic and thermal properties, let us consider a sequence of square (2D) representative unit cells with known relative density values θ_c' (Fig. 7). The size of the 2D unit cell is 20×20 (dimensionless length quantities). The finite element mesh is composed of Lagrange-type quadrialetral square (Q4) elements of size 1×1. Due to the symmetry of their structure, only $D^H_{c,1111}$, $D^H_{c,1122}$, $D^H_{c,1212}$, and $\kappa^H_{c,11}$ need to be computed as shown by Eqs. (6) and (13). Third-order polynomial approximations for $D^H_{c,1111}$, $D^H_{c,1122}$, $D^H_{c,1212}$, and $\kappa^H_{c,11}$ are defined according to Eqs. (15) and (16). The results are shown for unit elements Young's modulus and unit thermal conductivity so the approximation can be easily scaled (Fig. 7). Notably, the interpolations of the homogenized elastic properties $D^H_{c,ijkl}(\theta)$ are scaled by a factor of E_0 and the interpolation of the homogenized thermal conductivity $\kappa^H_{c,ij}(\theta)$ is scaled by a factor of κ_0.

5.1.2 Macroscale structural optimization

The macroscale structural optimization involves the solution of two problems. The first problem is stated in Eq. (27) and the second problem is stated in Eq. (31). In this example, $\theta_c^{\min} = 0.19$, $C_W = 2.0$, and $C_Q = 1.2$ are utilized. Table 1 summarizes the performance and topologies of the solid design $\boldsymbol{\theta}_0$, the solution of the first problem $\boldsymbol{\theta}_1^*$, and several solutions to the second problem $\boldsymbol{\theta}_2^*$. The solid design (row a) depicts the highest mass m, the lowest (best) mechanical compliance W and thermal compliance Q as well as the lowest maximum surface temperature T and lowest maximum displacement U.

The solution to the first problem (row b) has the lowest mass satisfying the mechanical and thermal compliance constraints. Since the material interpolation is linear, this design is conceptual but offers a reasonably good initial design for the second problem. Several solutions of the second problem are presented in Table 1 (rows c to k). Here, nonconvex functional constraints associated with U and T are implemented using $C_U = 1$ and $C_T = 1.05$; this is, no allowed increase in displacement and a five percent increase in temperature with respect to the solid design.

Without regularization ($C_R = 0$) and without penaliza-

tion ($C_P = 0$), the solution is binary (row c). This solution has the lowest mass $m(\boldsymbol{\theta}_2^*)$; however, it depicts thin-members that are difficult or impossible to capture in the additive manufacturing process. This drawback can be addressed with the use of the regularization function ($C_R = 0.001$) (row d). While the mass is increased with the respect to the previous design, the thin-members are no longer present. Unfortunately, there is a range of values of θ_c that cannot be captured in the additive manufacturing process due to the spatial material gradation.

Optimal manufacturable results (clustered designs) are achieved with the use of regularization ($C_R = 0.001$) and penalization ($C_P = 0.4$) functions. Table 1 includes solutions with two lattice phases (rows e to g), three lattice phases (rows h to j, and four lattice phases (row k). The predefined unit cells used in this problem are: $\theta_1' = 0.19$, $\theta_2' = 0.51$, $\theta_3' = 0.75$, and $\theta_4' = 1.00$ (solid phase). In these designs, W, Q, and U are active constraints. The constraint associated with T is inactive, hence the maximum temperature of these designs have small differences. For the optimization problem considered, the optimal design is the two-phase structure (row e) which has the lowest mass and satisfies all constraints; however, the haviest two-phase design (row g) may also be considered as an alternative since it has the lowest maximum temperature. With respect to the solid design, the optimal design (row e) reduces the mass in about 31.1% without increasing the maximum displacement, and increasing the maximum temperature in only about 2.0%.

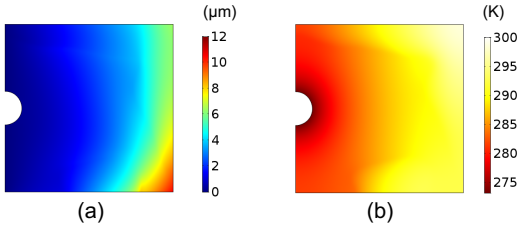

Fig. 8. Finite element analysis of the two-material, optimal design Table 1 (row e): (a) nodal displacement, and (b) nodal temperature distribution.

5.2 Design of a plastic injection mold

The proposed approach is applied to the optimal design of a multiphase, lattice plastic injection mold utilized for producing bump caps used in the car shock absorber. The injection mold consists of two main components: the cavity plate and the core plate. Each plate contains a solid volume comprising the surface in contact with the injected part. The mold is designed so that the injected part remains in the core plate and is ejected by ejection pins. The core plate is also referred to as the ejector mold. The geometries of the cavity and the core plates are shown in Fig. 9. During the optimization process the cooling channels and other orifices remain unchanged. The surfaces in contact with the cooling channels, orifices, and the injected part remain solid during the optimization process.

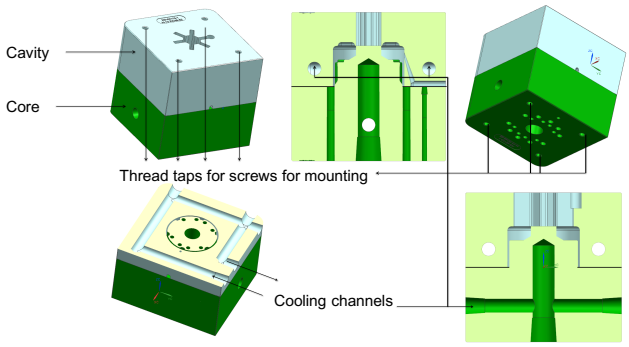

Fig. 9. The geometry of the original injection mold. Source: Hewitt Molding Company

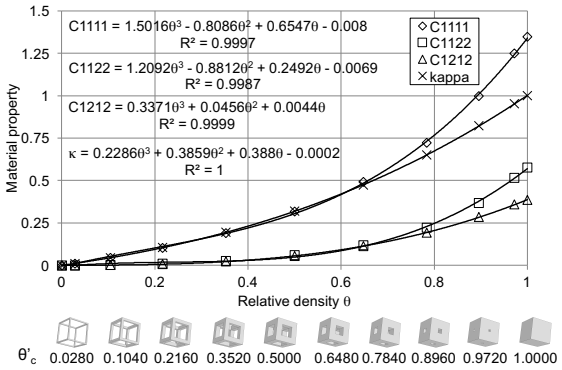

Fig. 10. Interpolation of elasticity coefficients and thermal conductivity for 3D unit cells.

5.2.1 Mesoscale analysis and homogenization

The homogenization of elastic and thermal properties makes use of cubic (3D) representative unit cells with relative densities θ_c' as shown in Fig. 10. For the analysis, each 3D unit cell is discretized into $20 \times 20 \times 20$ Lagrange brick elements. Due to the symmetry of the unit cell structure, only $D^H_{c,1111}$, $D^H_{c,1122}$, $D^H_{c,1212}$, and $\kappa^H_{c,11}$ need to be computed. Third-order polynomial approximations are defined according to Eqs. (15) and (16). The results are shown for unit elements Young's modulus and unit thermal conductivity so the approximation can be easily scaled (Fig. 10). A verification with respect to Hashin-Shtrikman (H-S) bounds for two-phase materials is shown in the Appendix.

5.2.2 Macroscale design of the cavity plate

The cavity plate is designed withing a design domain of dimensions 5.0 in $\times$ 5.0 in $\times$ 2.6 in (127 mm $\times$ 127 mm $\times$ 66 mm). This design domain is discretized into 97705 tetrahedral finite elements. The top surface of the cavity plate sustains a uniformly distributed load of 110 ton (1.08×10^6 N). Rollers are applied on the lateral surface nodes. The nodal displacement of the bottom surface is constrained in the z-direction. The injection pressure on the cavity is 131 MPa.

Table 1. Performance function values for the conceptual and final designs of the 2D plate.

Row	Design	$\boldsymbol{\theta}$	$m(\boldsymbol{\theta})$ [kg]	$W(\boldsymbol{\theta})$ [mJ]	$Q(\boldsymbol{\theta})$ [kg·m^2·K·s^{-3}]	$U(\boldsymbol{\theta})$ [μm]	$T(\boldsymbol{\theta})$ [K]
(a)	$\boldsymbol{\theta}_0 = \mathbf{1}$		78.500	1.871	114.75	0.278	288.00
(b)	$\boldsymbol{\theta}_1^*$	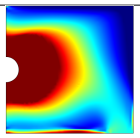	46.970	3.743	137.70	0.384	293.89
(c)	$\boldsymbol{\theta}_2^*(C_R = 0, C_P = 0)$		51.770	3.743	137.70	0.278	293.89
(d)	$\boldsymbol{\theta}_2^*(C_R = 0.001, C_P = 0)$	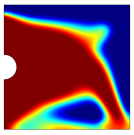	53.255	3.743	137.70	0.278	293.69
(e)	$\boldsymbol{\theta}_2^* \in \{\theta_1', \theta_4'\}(C_R = 0.001, C_P = 0.4)$		54.085	3.743	137.70	0.278	294.01
(f)	$\boldsymbol{\theta}_2^* \in \{\theta_2', \theta_4'\}(C_R = 0.001, C_P = 0.4)$	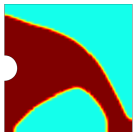	58.100	3.743	137.70	0.278	292.45
(g)	$\boldsymbol{\theta}_2^* \in \{\theta_3', \theta_4'\}(C_R = 0.001, C_P = 0.4)$		62.524	3.743	137.70	0.278	292.18
(h)	$\boldsymbol{\theta}_2^* \in \{\theta_1', \theta_2', \theta_4'\}(C_R = 0.001, C_P = 0.4)$	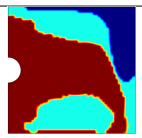	56.320	3.743	137.70	0.278	293.52
(i)	$\boldsymbol{\theta}_2^* \in \{\theta_1', \theta_3', \theta_4'\}(C_R = 0.001, C_P = 0.4)$		55.114	3.743	137.70	0.278	292.91
(j)	$\boldsymbol{\theta}_2^* \in \{\theta_2', \theta_3', \theta_4'\}(C_R = 0.001, C_P = 0.4)$	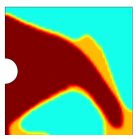	58.305	3.743	137.70	0.278	292.47
(k)	$\boldsymbol{\theta}_2^* \in \{\theta_1' \text{ to } \theta_4'\}(C_R = 0.001, C_P = 0.4)$	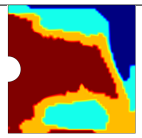	57.099	3.743	134.41	0.278	293.66

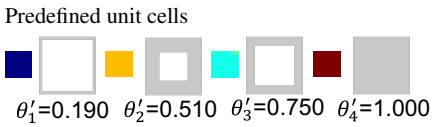

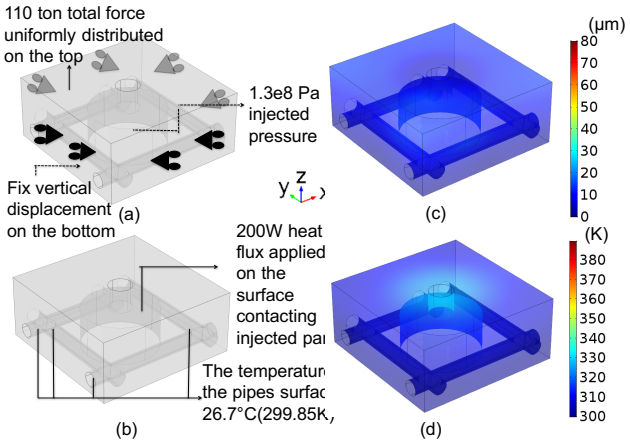

Fig. 11. Boundary conditions and results of the cavity plate's design domain with solid matrix: (a) mechanical loads and supports; (b) thermal heat flux and sink (cooling channel); (c) nodal displacement; and (d) nodal temperature distribution.

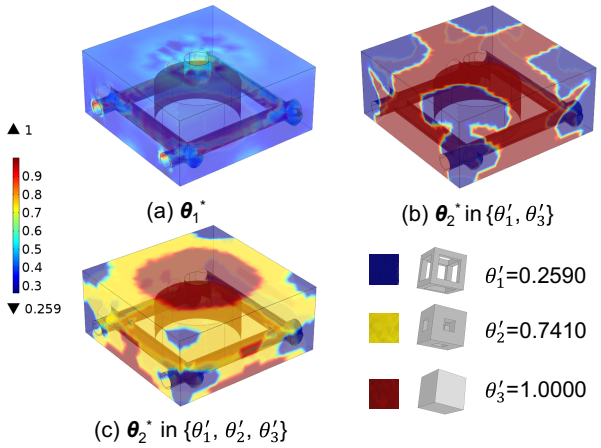

Fig. 12. The result optimal unit cell phases distribution of the design domain for the cavity plate.

Straight cooling channels are enclosed the injected part, and the temperature of the cooling channel surfaces is assumed to be 26.7 °C (299.9 K). In steady state, a heat flux of 200 W is imposed on the cavity. All other surfaces of the core are insulated (Fig. 11). The boundaries Γ_W and Γ_Q are defined as the cavity's surface in contact with the injected part. The nodal displacement and temperature distributions of the initial solid mold are shown in Fig. 11.

The design $\boldsymbol{\theta}_1^*$ corresponding to the solution of the first optimization problem Eq. (27) is shown in Fig. 12 (a). The performance of this design is summarized in Table 2 (row b). This conceptual design has the lowest mass m and satisfies the two functional constraints, i.e., mechanical compliance W and thermal compliance Q.

For the second problem Eq. (31), three predefined relative density values are used: $\theta_1' = 0.259$, $\theta_2' = 0.741$, and $\theta_3' = 1.000$ (solid phase). The parameters $C_P = 0.01$, $C_R = 0.03$, $C_U = 1$, and $C_T = 1.05$ are used in the optimization problem formulation. Here, two solutions $\boldsymbol{\theta}_2^*$ are presented Fig. 12 (b) and (c). These solutions consider two and three lattice phases, respectively. For these two designs, the constraints on W, Q, and U are activate, while the constraint on T is inactivate. Their performance is summarized in Table 2 (rows c and d). The two-phase design shows a 23.8% mass reduction with respect to the solid design. For the surface in contact with injected part, the maximum displacement remains the same and the maximum temperature increases 3.1%. The three-phases design has an improved (inactive) mechanical compliance and higher mass. Based on the problem statement, the two-phase design is preferred.

Table 2. Performance function values for the initial and final designs of the cavity

Row	Design	$m(\boldsymbol{\theta})$ [kg]	$W(\boldsymbol{\theta})$ [J]	$Q(\boldsymbol{\theta})$ [kg·m^2 ·K·s^{-3}]	$U(\boldsymbol{\theta})$ [μm]	$T(\boldsymbol{\theta})$ [K]
(a)	$\boldsymbol{\theta}_0 = \mathbf{1}$	5.275	12.78	3992.8	22.18	337.52
(b)	$\boldsymbol{\theta}_1^*$	3.112	25.55	4791.4	30.25	348.25
(c)	$\boldsymbol{\theta}_2^* \in \{\theta_1', \theta_3'\}$	4.072	25.55	4791.4	22.18	348.00
(d)	$\boldsymbol{\theta}_2^* \in \{\theta_1', \theta_2', \theta_3'\}$	4.086	23.80	4792.0	22.18	347.90

Table 3. Performance function values for the conceptual and final designs of the core.

Row	Design	$m(\boldsymbol{\theta})$ [kg]	$W(\boldsymbol{\theta})$ [J]	$Q(\boldsymbol{\theta})$ [kg·m^2 ·K·s^{-3}]	$U(\boldsymbol{\theta})$ [μm]	$T(\boldsymbol{\theta})$ [K]
(a)	$\boldsymbol{\theta}_0 = \mathbf{1}$	6.971	11.20	27037.0	16.95	481.92
(b)	$\boldsymbol{\theta}_1^*$	3.830	22.40	32444.4	15.05	507.84
(c)	$\boldsymbol{\theta}_2^* \in \{\theta_1', \theta_3'\}$	4.771	22.40	32444.4	14.63	502.10
(d)	$\boldsymbol{\theta}_2^* \in \{\theta_1', \theta_2', \theta_3'\}$	5.150	20.85	31652.2	15.61	501.94

5.2.3 Macroscale design of the core plate

The dimensions of the design domain for the core plate are 5.0 in × 5.0 in × 2.3 in (127 mm × 127 mm × 66 mm). The design domain is discretized into 113982 tetrahedral finite elements. The bottom surface of the core sustains a uniformly distributed load of 110 ton (1.08×10^6 N). Rollers are applied on the lateral surfaces. The displacement of the top surface is constrained in the z-direction. As before, the injection pressure on the interface between the part and the core is 131 MPa. The temperature on the surface of the cooling channel is set to be 26.7 °C (299.9 K). At the steady state, a heat flux of 200 W is imposed on the interface between the part and the core. All other surfaces of the core are insulated. The boundaries Γ_W and Γ_Q are defined as the plate's surface in contact with the part. The nodal displacement and temperature distributions of the initial solid mold are shown in Fig. 13.

The design $\boldsymbol{\theta}_1^*$ corresponding to the solution of the first

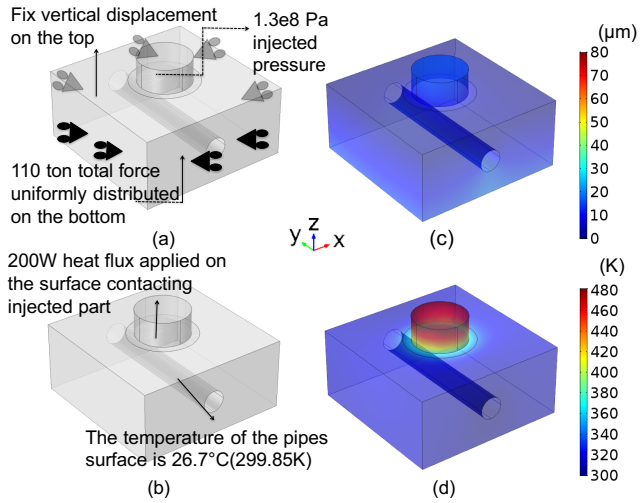

Fig. 13. Boundary conditions and FEA results of the core plate with solid matrix: (a) mechanical loads and supports; (b) thermal heat flux and sink (cooling channel); (c) nodal displacement; and (d) nodal temperature distribution.

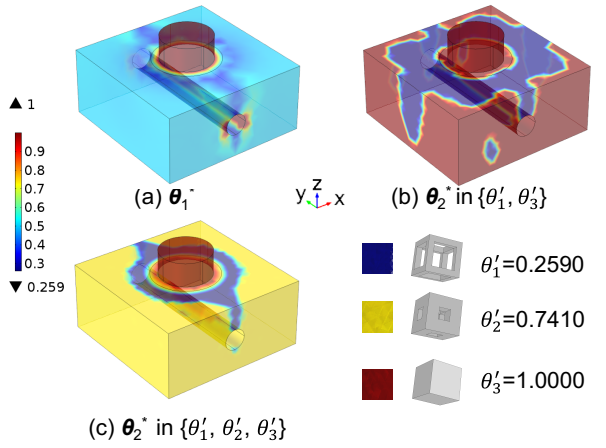

Fig. 14. The result optimal unit cell phases distribution of the design domain for the core plate.

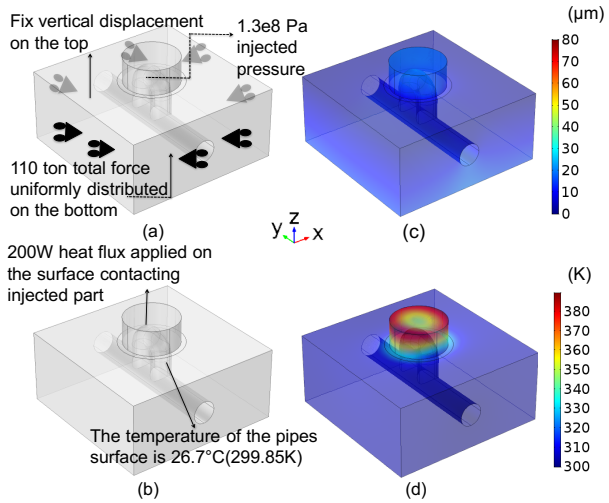

Fig. 15. Boundary conditions and FEA results of the core plate with solid matrix and conformal cooling channels: (a) mechanical loads and supports; (b) thermal heat flux, sink (cooling channel), and insulation; (c) nodal displacement; and (d) nodal temperature distribution.

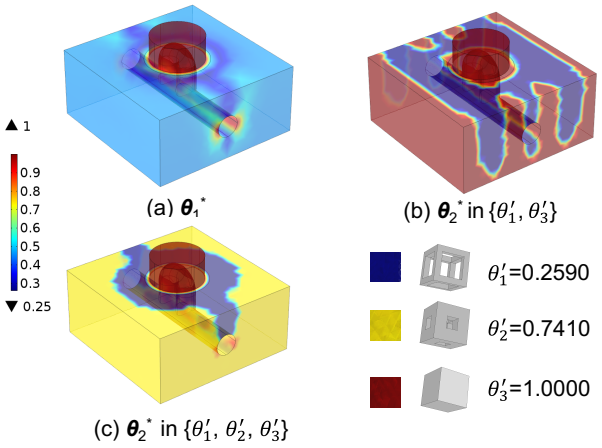

Fig. 16. The result optimal unit cell phases distribution of the design domain for the core plate with conformal cooling.

optimization problem, Eq. (27), is shown in Fig. 14 (a). The performance of this design is summarized in Table 3 (row b). As expected, this conceptual design has the lowest mass m and satisfies the functional constraints on mechanical compliance W and thermal compliance Q.

For the second problem, Eq. (31), the same three predefined relative density values are used, namely, $\theta_1' = 0.259$, $\theta_2' = 0.741$, and $\theta_3' = 1.000$ as well as the same parameters $C_P = 0.01$, $C_R = 0.03$, $C_U = 1$, and $C_T = 1.05$ in the optimization problem formulation. Two solutions $\boldsymbol{\theta}_2^*$ are presented Fig. 14 (b) and (c). These solutions consider two and three lattice phases, respectively. For these two designs, the constraints on W and Q are activate, while the constraint on U and T is inactivate. Their performance is summarized in Table 3 (rows c and d). The two-phase design shows a 31.6% mass reduction with respect to the solid design. For the surface in contact with injected part, the maximum displacement remains the same and the maximum temperature increases 4.2%.

5.2.4 Conformal cooling

In order to achieve better thermal performance, the proposed design approach can be applied to mold plates with conformal cooling channels. In this example, the straight cooling channel is replaced by a U-shaped cooling channel. This cooling channel conforms to the internal shape of the core plate as shown in Fig. 15. This modification significantly decreases the core plate's maximum temperature T and the thermal compliance Q without significantly change the maximum displacement U. As in the previous example, the two-phases design is the optimal solution. The FEA results are shown in Fig. 15 and summarized in Table 4.

Table 4. Performance function values for the conceptual and final designs of the core plate with conformal cooling.

Row	Design	$m(\boldsymbol{\theta})$ [kg]	$W(\boldsymbol{\theta})$ [J]	$Q(\boldsymbol{\theta})$ [kg·m^2 ·K·s^{-3}]	$U(\boldsymbol{\theta})$ [μm]	$T(\boldsymbol{\theta})$ [K]
(a)	$\boldsymbol{\theta}_0 = \mathbf{1}$	6.874	11.63	10966.0	19.92	388.18
(b)	$\boldsymbol{\theta}_1^*$	3.673	23.26	11325.7	18.95	389.61
(c)	$\boldsymbol{\theta}_2^* \in \{\theta_1', \theta_3'\}$	4.612	23.26	11205.1	14.91	388.85
(d)	$\boldsymbol{\theta}_2^* \in \{\theta_1', \theta_2', \theta_3'\}$	4.978	23.26	11452.9	15.61	389.27

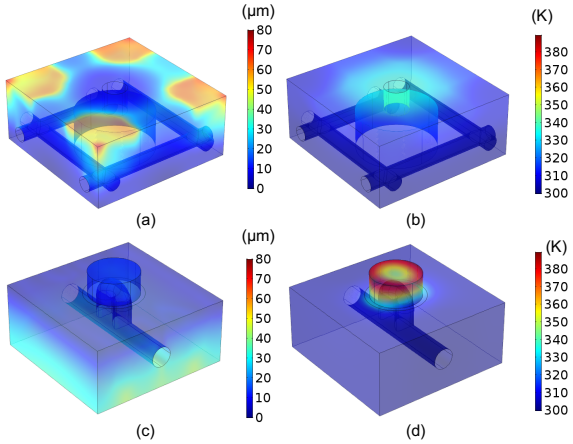

Fig. 17. Finite element analysis of the two-material optimal design: (a)The nodal displacement distribution of Table 2 (row c); (b) the nodal temperature distribution of Table 2 (row c); (c) the nodal displacement distribution of Table 4 (row c); and (d) the nodal temperature distribution of Table 4 (row c).

5.2.5 Additive Manufacturing

A prototype of the final lattice designs of the cavity and the core plates with conformal cooling channels are 3D-printed using a stereolithography (SLA) unit (Formlabs Form 2, Massachusetts). Clear resin is used to visualize the internal lattice structure and the conformal cooling channels (Fig. 18). The lattice structure is embodied by cubic lattice unit cells. The size of each cubic lattice unit cell is 0.2 in $\times$ 0.2 in $\times$ 0.2 in (5 mm $\times$ 5 mm $\times$ 5 mm). The minimum strut size and the minimum hole size within the unit cell are 0.067 in (1.7 mm). Experimental verification in the SLA unit shows that there is need for an internal support structure.

In order to demonstrated the feasibility for metal 3D-printing, a sample containing 125 graded cubic lattice unit cells (5 $\times$ 5 $\times$ 5) is designed and printed in a Direct Metal Laser Sintering (DMLS) unit (EOS M280, Hamburg, Germany) (Fig. 18 g). The test shows that without internal support structure, the quality of any lattice cube with strut and hole size greater than 0.03 in (0.762 mm) is guaranteed: smaller strut members may curl during and smaller holes may be completely filled during the prining process. This experimental test demonstrates the optimal design can be 3D-printed without internal support structure.

6 Conclusion

This work presents a multiphase thermomechanical design approach to obtain lightweight thermomechanical cellular components such as lattice injection molds. The final lattice structures are suitable for additive manufacturing. The (mesoscale) lattice unit cell thermomehanical properties are derived using asymptotic homogenization. A polynomial fitting function is conveniently defined in order to conduct the (macroscale) structural optimization. The optimal macroscale design is obtained through thermomechanical, FEA-based structural optimization.

The proposed approach allows the systematic optimal design of lightweight lattice structures satisfying the global and local mechanical and thermal constraints. The optimal structure is defined by the optimal distribution of predefined lattice unit cells. The numerical examples show that a small reduction in mechanical and thermal performance allows for significant mass savings, which translate into manufacturing cost saving. This approach is suitable for additive manufacture process.

Ongoing work focuses on the thermal and mechanical experimental tests. In addition, the influence of the lattice unit cell's architecture on the additive manufacturing cost and feasibility will be investigated. Finally, rather than assuming the constant temperature on the surface of the pipe, effort should be devoted on including heat convection and advection effects in pipe flows in the future design. To improve the steady state analysis, cooling cycles of the optimal design may be investigated.

Acknowledgements

The Walmart Foundation supported this research effort. Hewitt Molding Company (Kokomo, Indiana) provided the original injection mold model for the investigation. 3D Part Manufacturing (Indianapolis, Indiana) 3D-printed the metal specimens. Any opinions, findings, conclusions, and recommendations expressed in this investigation are those of the writers and do not necessarily reflect the views of the sponsors.

References

[1] Wang, G., Zhao, G., and Guan, Y., 2013. "Thermal response of an electric heating rapid heat cycle molding mold and its effect on surface appearance and tensile strength of the molded part". *Journal of Applied Polymer Science,* **128**(3), pp. 1339–1352.

[2] Sundarram, S. S., Jiang, W., and Li, W., 2014. "Fabrication of small pore-size nickel foams using electroless plating of solid-state foamed immiscible polymer blends". *Journal of Manufacturing Science and Engineering,* **136**(2), p. 021002.

[3] Barletta, M., Gisario, A., Guarino, S., and Rubino, G., 2009. "Production of open cell aluminum foams by using the dissolution and sintering process (dsp)". *Journal of Manufacturing Science and Engineering,* **131**(4), p. 041009.

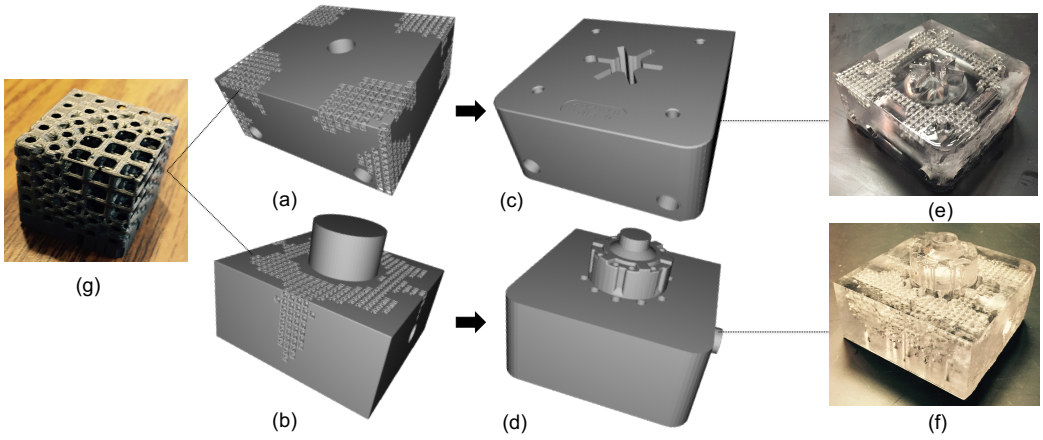

Fig. 18. (a) The lattice structure of the design domain of the cavity; (b) The lattice structure of the design domain of the core; (c) The final design of the cavity; (d) The final design of the core; (e)The final design of the cavity printed by Formlab Form 2 printer; (f) The final design of the core printed by FORMLAB SLA printer;(g) A lattice structure sample printed by DMLS EOS M280.

[4] Conley, J., and Marcus, H., 1997. "Rapid prototyping and solid free form fabrication". *Journal of Manufacturing Science and Engineering,* **119**(4B), pp. 811–816.

[5] Tsopanos, S., Mines, R., McKown, S., Shen, Y., Cantwell, W., Brooks, W., and Sutcliffe, C., 2010. "The influence of processing parameters on the mechanical properties of selectively laser melted stainless steel microlattice structures". *Journal of Manufacturing Science and Engineering,* **132**(4), p. 041011.

[6] Parthasarathy, J., Starly, B., and Raman, S., 2011. "A design for the additive manufacture of functionally graded porous structures with tailored mechanical properties for biomedical applications". *Journal of Manufacturing Processes,* **13**(2), pp. 160–170.

[7] Gaynor, A. T., Meisel, N. A., Williams, C. B., and Guest, J. K., 2014. "Multiple-material topology optimization of compliant mechanisms created via polyjet three-dimensional printing". *Journal of Manufacturing Science and Engineering,* **136**(6).

[8] Zegard, T., and Paulino, G. H., 2015. "Bridging topology optimization and additive manufacturing". *Structural and Multidisciplinary Optimization*.

[9] Dede, E. M., Nomura, T., and Lee, J., 2014. *Multiphysics Simulation*. Springer.

[10] Gao, T., Zhang, W., Zhu, J., Xu, Y., and Bassir, D., 2008. "Topology optimization of heat conduction problem involving design-dependent heat load effect". *Finite Elements in Analysis and Design,* **44**(14), pp. 805–813.

[11] Koga, A. A., Lopes, E. C. C., Nova, H. F. V., de Lima, C. R., and Silva, E. C. N., 2013. "Development of heat sink device by using topology optimization". *International Journal of Heat and Mass Transfer,* **64**, pp. 759–772.

[12] Wu, T., Jahan, S. A., Kumaar, P., Tovar, A., El-Mounayri, H., Zhang, Y., Zhang, J., Acheson, D., Brand, K., and Nalim, R., 2015. "A framework for optimizing the design of injection molds with conformal cooling for additive manufacturing". *Procedia Manufacturing,* **1**, pp. 404–415.

[13] Coelho, P. G., Cardoso, J. B., Fernandes, P. R., and Rodrigues, H. C., 2011. "Parallel computing techniques applied to the simultaneous design of structure and material". *Advances in Engineering Software,* **42**(5), pp. 219–227.

[14] Zhang, P., Toman, J., Yu, Y., Biyikli, E., Kirca, M., Chmielus, M., and To, A. C., 2015. "Efficient design-optimization of variable-density hexagonal cellular structure by additive manufacturing: Theory and validation". *Journal of Manufacturing Science and Engineering,* **137**(2), p. 021004.

[15] Andreassen, E., and Jensen, J. S., 2015. "A practical multiscale approach for optimization of structural damping". *Structural and Multidisciplinary Optimization*, pp. 1–10.

[16] Gersborg-Hansen, A., Bendsøe, M. P., and Sigmund, O., 2006. "Topology optimization of heat conduction problems using the finite volume method". *Structural and multidisciplinary optimization,* **31**(4), pp. 251–259.

[17] Hassani, B., and Hinton, E., 1998. "A review of homogenization and topology optimization. ii. analytical and numerical solution of homogenization equations". *Computers and Structures,* **69**(6), pp. 719 – 38.

[18] Andreassen, E., and Andreasen, C., 2014. "How to determine composite material properties using numerical homogenization". *Computational Materials Science,* **83**, pp. 488 – 95.

[19] Song, Y. S., and Youn, J. R., 2006. "Evaluation of effective thermal conductivity for carbon nanotube/polymer composites using control volume finite element method". *Carbon,* **44**(4), pp. 710–717.

[20] Svanberg, K., 2007. Mma and gcmma-two methods for nonlinear optimization. Tech. rep., Technical report.
[21] Borrvall, T., 2001. "Topology optimization of elastic continua using restriction". *Archives of Computational Methods in Engineering,* **8**(4), pp. 351–385.
[22] Hashin, Z., and Shtrikman, S., 1962. "A variational approach to the theory of the effective magnetic permeability of multiphase materials". *Journal of applied Physics,* **33**(10), pp. 3125–3131.
[23] Hashin, Z., and Shtrikman, S., 1963. "A variational approach to the theory of the elastic behaviour of multiphase materials". *Journal of the Mechanics and Physics of Solids,* **11**(2), pp. 127–140.

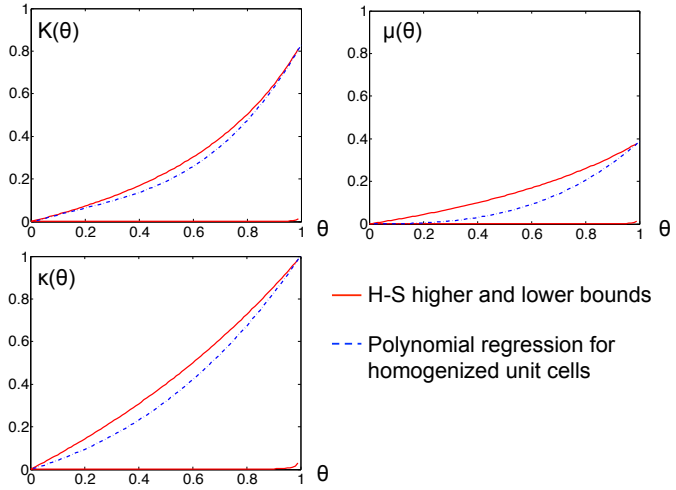

Fig. 19. The comparision between continuous 3D unit cells properties derived by polynomial regression and Hashin-Strikman bounds.

Appendix 1: Verification of the homogenization using Hashin-Shtrikman bounds

For verification of the homogenization and interpolation procedures, let us consider lattice unit cells using linear elasticity and thermal conductivity theories. The bulk modulus is given by

$$\begin{aligned} K(\theta) = \; & D^H_{c,1111}(\theta) - \tfrac{4}{3} D^H_{c,1212}(\theta) \\ = \; & D^H_{c,1122}(\theta) - \tfrac{2}{3} D^H_{c,1212}(\theta), \end{aligned} \tag{32}$$

the shear modulus is given by

$$\mu(\theta) = D^H_{c,1212}(\theta), \tag{33}$$

and thermal conductivity is given by

$$\kappa(\theta) = \kappa^H_{c,1}(\theta). \tag{34}$$

The bulk modulus, shear modulus, and thermal conductivity are compared with the Hashin-Shtrikman (H-S) bounds for two-phase materials [22, 23]. Figure 19 represents H-S bounds and functions corresponding to the 3D unit cells. As expected, the polynomial approximations falls within the H-S bound, closer to the upper bound.